Key Role of Defects in Thermoelectric Performance of TiMSn (M = Ni, Pd, and Pt) Half-Heusler Alloys

Atreyi Dasmahapatra, Loredana Edith Daga, Antti J. Karttunen, Lorenzo Maschio,* and Silvia Casassa*

Cite This: *J. Phys. Chem. C* 2020, 124, 14997−15006 | Read Online

ACCESS | Metrics & More | Article Recommendations | Supporting Information

ABSTRACT: Half-Heusler alloys are thermoelectric materials that enable direct conversion of waste heat to electricity. A systematic study of these alloys has never been attempted using local Gaussian type orbitals (GTOs) and hybrid density functional theory methods within a periodic approach. In this work, we study the thermoelectric properties of TiMSn (M = Ni, Pd, and Pt) alloys with space group $F\bar{4}3m$ using the CRYSTAL code. We, first, set benchmarks for TiNiSn by comparing our data to existing literature values of Seebeck coefficient, power-factor, and thermoelectric figure-of-merit. Our results agree well. We, then, extend these calculations to TiPdSn and TiPtSn, for which consistent previous data are limited. Our computations show that all TiMSn (M = Ni, Pd, and Pt) alloys prefer p-type carriers and exhibit a figure-of-merit of ≈1 at a chosen carrier concentration and temperature. In addition, we aim to explain the low band-gap of TiNiSn by modeling defects in the pure system. Our defect model proves to have a smaller band-gap, and its power-factor is found to be almost twice of the pure TiNiSn.
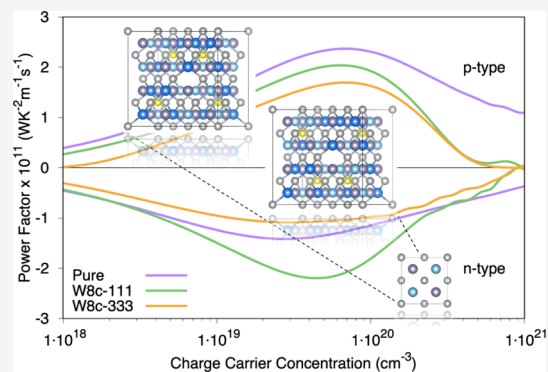
1. INTRODUCTION

The term thermoelectrics (TEs) has sparked huge interest in recent years, as the perspective of turning waste heat into useful electricity grows in the light of renewed attention toward the environment. From electric cars to wearable devices, and thereon up to space exploration, the horizon of reducing energy demands seems to be at hand. Unfortunately, because of their modest efficiency and relatively high cost, currently available devices and materials are not able to deliver this promise.

Compared to other fields of solid-state physics and materials chemistry, the alliance of theoretical modeling, experimental characterization, and synthesis is not prevalent in TEs. Plausible reasons are that for an experimentally synthesized sample, there is a high density of defects (interstitial, substitutional, etc.) that provide a high carrier density. Despite the crystalline nature of the compound, realistic models that integrate these defects are difficult to mimic. Moreover, grain boundaries found in real materials are beneficial to TE properties as they reduce the thermal conductivity of the sample, but these structural defects are also complicated to integrate in a model.

As C. J. Humphreys once quoted: "Crystals are like people: it is the defects in them which tend to make them interesting!".[1] For TEs, this is indeed the case, as the presence of interstitial or substitutional defects not only adds flat bands in the gap but also alters the shape of a large part of the band structure.

Half-Heusler (HH) alloys, intermetallic compounds of the composition ABX, are now actively investigated for their TE performance. These compounds have tunable band gaps which allow the possibility of tailoring TE efficiency and have potential applications in spintronics, solar cells, and data storage.[2−4]

Experimentally, these materials are synthesized using various methods: spark plasma sintering, hot pressing, arc-melting, and microwave-assisted solid-state reactions. These methods are generally followed by prolonged annealing that is targeted to densify the material and heal the sample of defects.[5−8]

On computational side, a recent impetus in the investigation of these alloys is to use machine learning tools to accelerate the discovery of new novel materials.[9−11] The primary focus, however, is doping the parent material to maximize the TE power factor σS^2 and in turn the TE figure of merit ($ZT = S^2\sigma T/k_{total}$, where k_{total} is the material's total thermal conductivity). This approach comes from the general idea that adding impurities (doping or substituting by isoelectronic elements) alters the band gap of the parent material, which in turn enhances the TE properties.[12−17] The changes in the
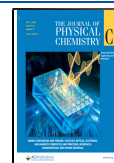
atomic bonding in the proximity of the grain boundaries and the consequent covalent bond delocalization can also deeply modify the TEs, thus stimulating the electron transport of the whole system.[18]

In this paper, we investigate three TE compounds, TiNiSn, TiPdSn, and TiPtSn, with the CRYSTAL code,[19] using hybrid density functional methods and basis sets of localized Gaussian orbitals. Such computational setup, if properly tuned, enables the inclusion of exact exchange at a relatively cheap computational cost, allowing for a natural reduction of self-interaction effects. Moreover, it can be more accurate and robust with respect to other density functional theory (DFT) approaches that use Hubbard-U corrected functionals for defects and HH alloys.[20,21] Our work is targeted toward confirming how, contrary to other materials, point defects in HH alloys have a strong impact on the whole band structure and consequently on transport properties. Moreover, we intend to benefit the community that uses Gaussian type orbitals in the study of crystalline materials, by establishing a reliable methodology and providing an integrated tool to compute TE properties within the CRYSTAL code.[22] Among HH alloys, TiNiSn is heralded as a benchmark material and is well investigated in the literature. Thus, naturally, we first compare our data for TiNiSn to the existing literature, validate both the approach and the computational setting, and then extend the same machinery to investigate TiPdSn and TiPtSn.

The paper is arranged as follows: in the following section, the computational setup is described, in particular, the reasoning for our choice of basis-sets and DFT functionals. Results are presented in Section 3, where the variance of the band gap and reproducibility of the band structure depending on the choice of functionals are studied. Thereafter, a discussion of TE properties with appropriate comparison to the existing literature is provided. In the last section, we present a defect model of TiNiSn that shows improved TE performance.

2. METHODS

2.1. Functional and Basis Set. Throughout this work, we apply DFT as implemented in the CRYSTAL code.[19]

While most studies with TEs employ plane-wave based packages and the Perdew−Burke−Ernzerhof (PBE) functional,[23] the local basis in CRYSTAL allows us to introduce a proper amount of 'exact exchange' which is known to improve the accuracy of simulated properties that depend on the extent of electronic delocalization, namely, band gaps, phonon spectra, and magnetic coupling constants.[24]

Nevertheless, atomic basis sets, which allow for an easy use of hybrid functionals, have to be accurately calibrated for periodic systems, and the correct percentage of exact exchange has to be determined.

In order to define a reference setup, which predicts the best compromise of the electronic band gap and lattice parameter for the family of systems under investigation, we perform a comprehensive screening in the choice of the basis sets and on the amount of Hartree−Fock (HF) exchange.

For the basis, we adopt a standard and rather robust procedure to adapt molecular Karlsruhe split-valence polarization basis (def2-SVP) to periodic calculations.[25] A consistent basis set, referred in the following as $P.def2\text{-}SVP$, is obtained by cutting off f functions, when present, and adjusting the outermost s and p shells for periodic calculations, also using the BDIIS optimization procedure.[26] For each

element included here, the basis set has been used successfully in previous studies. The basis sets and the literature references are reported in Supporting Information.

For the functional, we explore PBE with three different percentages of HF exchange, namely, pure PBE, PBE10 (10% HF exchange) and PBE0 (25% of exact exchange[23,27,28]). On the basis of our results, we resolved to use the hybrid PBE10 for all further computation. It is to be noted here that calculations with PBE are reported for sake of comparison with literature results.

2.2. Computational Parameters. The DFT exchange−correlation contribution is evaluated by numerical integration over the unit cell volume, using a pruned grid with 75 radial and 974 angular points. Integration over the reciprocal space is carried out using Monkhorst−Pack meshes of $8 \times 8 \times 8$. The Coulomb and exchange series, summed in direct space, are truncated using overlap criteria thresholds of $[8, 8, 8, 8, 16]$. Convergence for the self-consistent field algorithm is achieved up to a threshold of 10^{-9} hartree on the total energy, per unit cell.[29]

Geometry optimization is performed using analytical gradients with respect to atomic coordinates and unit−cell parameters, within a quasi-Newtonian scheme combined with Broyden−Fletcher−Goldfarb−Shanno Hessian updating.[30,31] The default convergence criteria are adopted for both gradient components and nuclear displacements. A full set of vibrational frequencies in Γ is obtained within the harmonic approximation by diagonalizing the mass-weighted Hessian matrix. This matrix is built by numerically differencing the analytical gradient with respect to atomic Cartesian coordinates. The zero-point energy (ZPE) and the thermal contributions to the vibrational energy (E_{vib}) and entropy (S_{vib}) are calculated by considering the vibrational spectrum in Γ and then added to the SCF energy and the pressure x volume term to get all the thermodynamic potential, that is, enthalpy and Gibbs free energy, at any given temperature.

TE properties such as Seebeck coefficient (S) electrical conductivity (σ) and electron contribution to the thermal conductivity (k_{el}) are computed by using the semi-classical Boltzmann transport equation theory and the frozen band approximation, as recently implemented by Sansone et al. in CYRSTAL.[22] We also assume constant relaxation time approximation for carriers and fix it at 10 fs (1×10^{-14} s) for all systems and temperatures. A dense mesh of up to 4000 k-points is used in the first Brillouin zone for the calculation of TE parameters. Our computations do not include the effect of spin−orbit coupling as this feature is yet to be implemented in the CRYSTAL code.

Thus, we do our computations within the regime of the CRYSTAL code, using carefully screened localized Gaussian type orbitals and hybrid DFT functionals to describe the chemistry of the HH alloys. Once a reliable computational setting is achieved, features of the code which can then be exploited are (i) calculation of the TE parameters for different carrier-concentrations, at various temperatures and at low computational cost; (ii) chemical insight into the electronic structure because of the atomic nature of the basis set; and (iii) modeling of low concentration of point defects using a supercell approach.

3. RESULTS AND DISCUSSION

3.1. Defect-Free Crystal Structure. The HH pure-phase crystallizes in a MgAgAs-type structure with space group $F\bar{4}3m$

(#216). Similar to other ternary HH alloys, Sn, Ni/Pt/Pd, and Ti atoms occupy fused face-centered cubic sublattices at Wyckoff positions of $4b$ [1/4, 1/4, 1/4], $4c$ [1/2, 1/2, 1/2], and $4a$ [0, 0, 0], respectively. A representative model is shown in Figure 1.
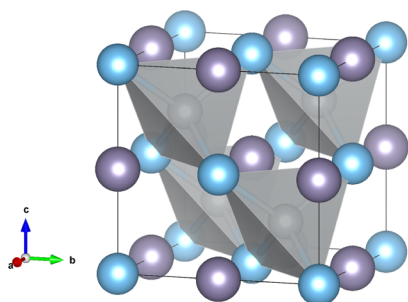
Figure 1. HH structure of TiMSn (M = Ni, Pt, and Pd) alloy with cubic symmetry and space group $F\bar{4}3m$ (#216). Blue spheres are Ti atoms, grey spheres in polyhedra are Ni, Pd, and Pt (for each case), and purple spheres are Sn atoms.

Structural parameters and electron band gap, calculated at the PBE10/$P.def2$-SVP level, are collected in Table 1. The equilibrium Bulk modulus, B_0, elastic constants, c_{11}, c_{12}, c_{44}, Poisson ratio, ν, and Young's modulus, Y, are obtained with CRYSTAL by solving the third-order Birch−Murnaghan isothermal equation of state.[32]

For the lattice parameter, a, our finding for TiNiSn deviates from an experiment value of a negligible 0.2%,[33,34] whereas TiPdSn and TiPtSn values are in accordance to those in refs 9 and 35, respectively. Band gaps will be discussed in the next section.

In the case of TiNiSn, the elastic properties are reproduced accurately even though our perfect crystal model is not completely consistent with realistic experimental samples, where local and structural defects are always present. Hence, a good agreement is achieved for Young's modulus, but significant discrepancies are observed for B_0 and the elastic constants.

In the absence of experimental data for TiPdSn and TiPtSn alloys, we compared our calculations with results obtained with a plane-wave approach reported by Kaur[35] and Roy et al.,[36] respectively. As shown in Table 1, the agreement for TiPdNi's B_0 and TiPtSn's c_{44} elastic constant is excellent.

3.2. Defect-Free Electronic Band Structure. For a complete discussion of TE properties of HH compounds, a correct description of the electronic band structure of the material is essential. In Figure 2, we show the band structures of all three ternary compounds computed at the PBE10/$P.def2$-SVP level.

As expected, each compound has an indirect band gap, between the valence-band maximum at the Γ-point and the conduction-band minimum at **X**-point. The percentage of exact exchange in the functionals does affect the numerical value of the band gap. For instance, for TiNiSn, the band-gap varies from 0.48 eV (PBE) to 0.69 eV (PBE10) and finally to 0.98 eV (PBE0). Nevertheless, none of the functionals produce the band gap as low as the experimentally measured value of 0.12 eV.[37] We discuss this anomaly in detail in the following.

For TiPdSn, our computed band gap is 0.76 eV (0.47 eV with PBE) which matches with previous calculations done using the range-separated hybrid HSE06 functionals.[9] TiPtSn has the highest band gap of the three alloys at 1.13 eV (0.72, PBE) which is ≈10% less than the literature value obtained with the HSE06 functional.[9]

For the band structure, the primary difference between the three compounds is at the **X**-point. Going from Ni−Pd−Pt, the splitting between the two lowest energy conduction bands reduces, increasing the band gap. These bands have a pudding mold-like character, which is more pronounced in the case of TiNiSn.

The projected density of states (PDOS) on the atomic orbitals of each element can enlighten more on this important effect. The lowest virtual states of TiNiSn, panel (a) of Figure 3, result as a combination of Ni−Ti AOs and are slightly closer to the Fermi level with respect to the analogous Pd/Pt−Ti states in the other two alloys. This is the primary reason behind why the electronic band gap increases as we go from TiNiSn to TiPtSn because the Sn contribution in the Fermi region is almost negligible for all three compounds.

3.3. Defect-Free TE Properties. We now discuss the Seebeck coefficient (S), the electrical conductivity (σ), and the power factor with respect to the relaxation time (PF = $S^2\sigma/\tau$) for these HH alloys. Because TE materials have high temperature applications, we also present the dependence of these parameters at temperatures, from 300 to 1000 K. We first compute TE properties of TiNiSn and compare it with existing literature, both from computational and experimental studies, to establish a benchmark. Later, we extend the same calculations to TiPdSn and TiPtSn, on which computational data are sparse.

Figure 4 compares S and power-factor for TiNiSn with change in charge carrier concentration (n_c) for both p and n-type carriers adopting the PBE and PBE10 functionals. At low n_c, the Seebeck coefficient differs slightly between PBE and PBE10, but as n_c increases, S quickly converges. For higher temperatures (not shown here) difference between S is almost

Table 1. PBE10/$P.def2$-SVP Results for Three HH Alloys[a]

| alloy	a	gap	B_0	c_{11}	c_{12}	c_{44}	ν	Y
TiNiSn	5.91	0.69	137.94	235.53	89.98	60.97	0.296	169.62
Ref.	5.92[b]	0.12[c]	124.90[d]	214.90[d]	79.90[d]	67.50[d]	0.271[d]	171.6[d]
TiPdSn	6.17	0.76	131.21	184.96	105.27	58.97	0.330	134.11
Ref.	6.23[e,f]	0.74[e]	135.90[f]					
TiPtSn	6.22	1.13	146.02	206.96	116.85	65.89	0.329	150.42
Ref.	6.25[e]	1.31[e]	67.00[g]					

[a]Lattice parameter a in Å. Indirect electronic band gap in eV. Bulk modulus, B_0, elastic contants, c_{11}, c_{12}, c_{44}, Young's modulus, Y, in GPa and Poisson ratio, ν. Literature date ara reported when available. [b]Ref 34, (EXP). [c]Ref 37, (EXP). [d]Ref 38, (EXP). [e]Ref 9, (THEO). [f]Ref 35, (THEO). [g]Ref 36, (THEO).
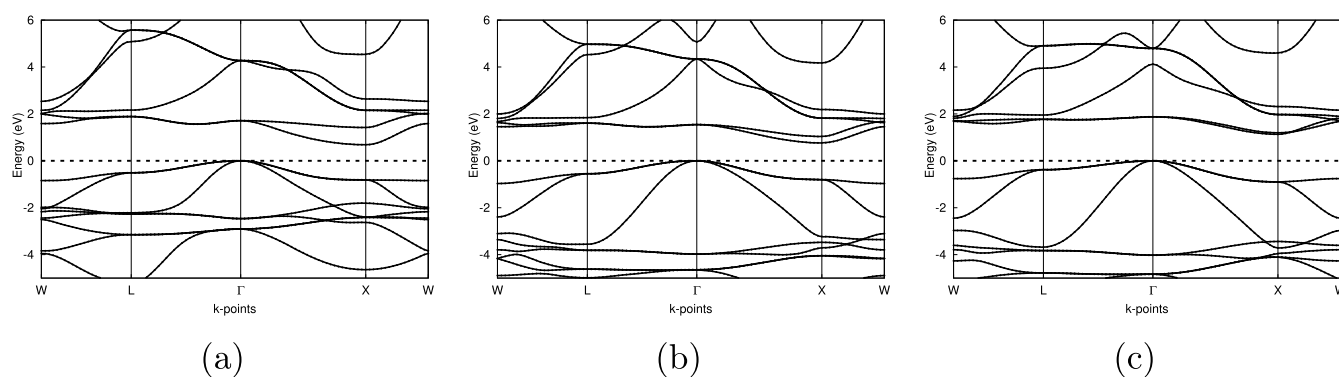
Figure 2. Computed electronic band structures for (a) TiNiSn, (b) TiPdSn, and (c) TiPtSn at the PBE10/*P.def 2-SVP* level. Indirect band gaps are 0.69, 0.76, and 1.13 eV (from left to right) between the Γ and X point. Dotted line corresponds to the Fermi energy.
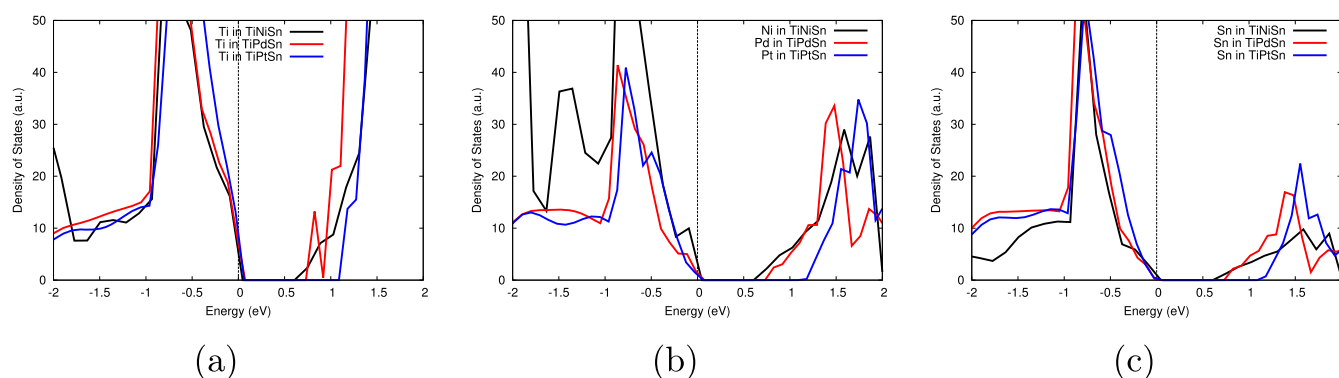
Figure 3. Computed PDOS on the atomic orbitals of (a) Ti, (b) Ni/Pd/Pt, and (c) Sn, at the PBE10/*P.def 2-SVP* level. Dotted line corresponds to the Fermi energy.
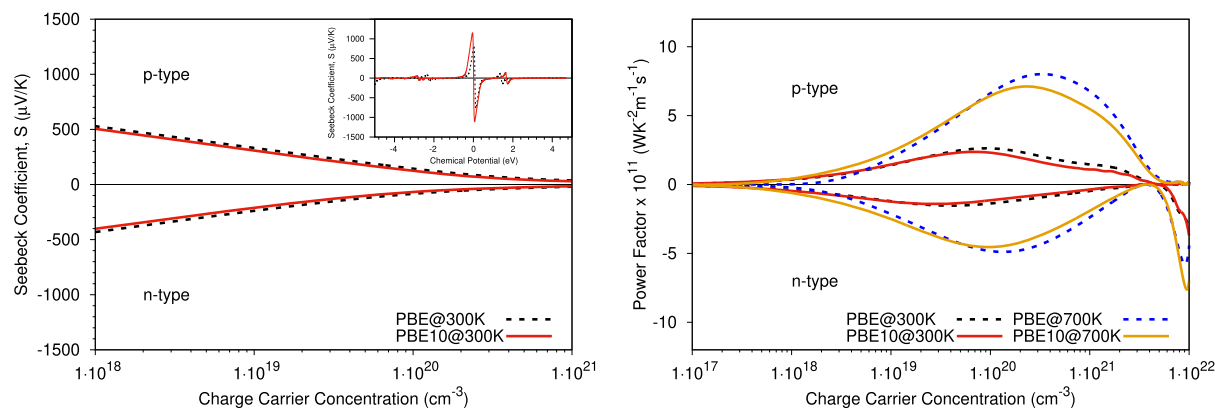
Figure 4. (left) Seebeck coefficient for TiNiSn obtained with PBE10 (solid line, red) and PBE (dotted line, black) for both p-type and n-type doping plotted against carrier concentration at 300 K. Inset: Variance of Seebeck coefficient with change in chemical potential (μ), in eV. (right) Power-factor (PF, $S^2\sigma/\tau$) with respect to relaxation time (τ) of carriers, for p-type and n-type doping with change in n_c at T = 300 K (solid line, red: PBE10 and dotted line, black: PBE) and T = 700 K (solid line, orange: PBE10 and dotted line, blue: PBE). The *x*-axis for the figure on the right is extended to 1×10^{17} for ease of comparison between the functionals. S and PF with n-carriers are plotted on the negative axis for clarity.

negligible. On the contrary, PF is lightly more sensitive to HF percentage at high n_c values, but its main features are the same with the two functionals.

Overall, our computations match the general trend of large Seebeck values for TiNiSn and provide good agreement with existing literature at specified charge carrier concentrations.

In particular, the highest reported value of S for TiNiSn found through computational and experimental studies in literature is ≈ -250 μV/K, which we achieve for $n_c \sim 1 \times 10^{19}$ cm^{-3}.[39-41] Scanning at the lower carrier concentration ranges of $n_c \sim 1 \times 10^{18}$ cm^{-3}, we have $S = -400$ μV/K, which

corresponds to the work done by Zilber et al.,[42] who reported a value of $S = -425 \pm 50$ μV/K with $n_c \sim 7 \times 10^{18}$ cm^{-3}.

The power-factor dependency on temperature is correctly reproduced because it increases from ≈ 2 to ≈ 7 W/ms K$^2 \times 10^{11}$ as the temperature increases from 300 to 700 K, in agreement with the results reported by Wang et al.[43]

At 300 K, the maximum value of PF for p-type carriers is 2.2 W/m K$^2 \times 10^{11}$ corresponding to $n_c \sim 1 \times 10^{20}$ cm^{-3} and $S = +124$ μV/K, while for n-type, the highest power-factor is 1.2 W/m K$^2 \times 10^{11}$, with $S = -103$ μV/K, achieved when $n_c \sim 5 \times 10^{19}$ cm^{-3}.
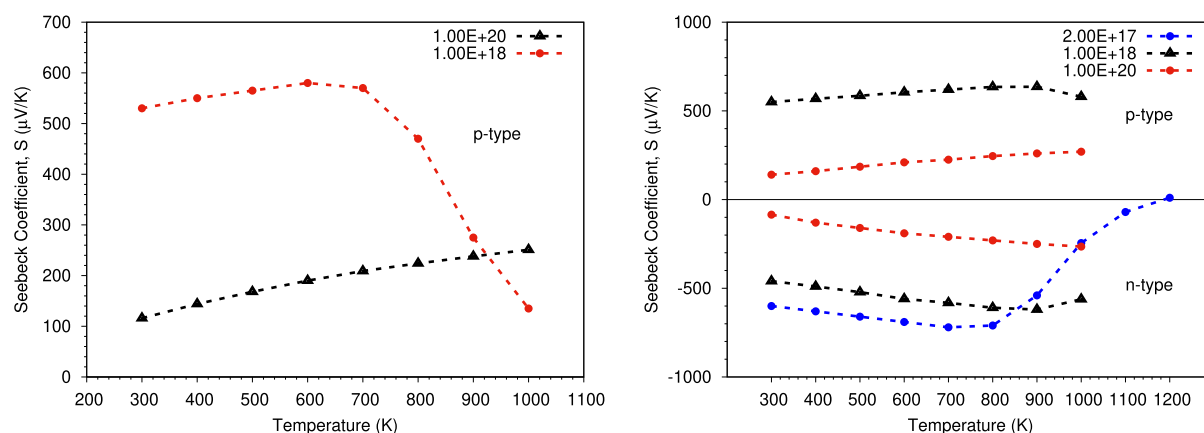
Figure 5. Temperature dependence of Seebeck coefficient. (left) TiPdSn, $n_c = 1 \times 10^{18}$ (red circles) and $n_c = 1 \times 10^{20}$ (black triangles) cm^{-3} for p-type doping. (right) TiPtSn, $n_c = 2 \times 10^{17}$, $n_c = 1 \times 10^{18}$ and $n_c = 1 \times 10^{20}$ cm^{-3} for both p and n-type doping. Calculations performed at the PBE10/P.def2-SVP level.

Our computations suggest that p-type doping results in higher TE efficiency in TiNiSn and this is particularly evident at $n_c \sim 1 \times 10^{19}$ cm^{-3}, where PF for p-type is almost double than for n-type, right panel of Figure 4. For most experimental data, TiNiSn is recognized to favor n-type doping. However, as Zilber et al. propose, the electron donor levels arising from grain boundaries in polycrystalline TiNiSn samples can be reduced to single-crystals to attain the p-type TiNiSn TE.[42]

Convinced that our methodology to compute TE parameters yields satisfactory results for HH compounds, we now extend the same setup for the study of TiPdSn and TiPtSn. As mentioned earlier, for these compounds, reliable computational or experimental studies are limited.

In Figure 5, we plot variation of Seebeck coefficient for TiPdSn with temperatures at two values of $n_c \sim 1 \times 10^{18}$ and $n_c \sim 1 \times 10^{20}$ cm^{-3} (left) and for TiPtSn at $n_c \sim 2 \times 10^{17}$, 1×10^{18} and 1×10^{20} cm^{-3} (right).

Maximum power factor in both cases is achieved considering p-type carriers, see Table 2, at $n_c \sim 1 \times 10^{20}$ cm^{-3}.

However, for TiPdSn at 300 K, our value of $S = +116$ μV/K is half of the value suggested by Kaur ($S = +320$ μV/K).[35] We believe that this discrepancy arises from the different lifetime adopted in ref 35 that is 30 times larger compared to our current work. As regards the dependence on temperature of the Seebeck coefficient, the trend change as a function of the carrier concentration, that is, for $n_c \sim 1 \times 10^{18}$ cm^{-3} S, exhibits an increasing with temperature until 700 K and then a steep decrease until 1000 K, whereas at higher n_c (black curve of the left panel, Figure 5), S monotonously rises on increasing temperature.

In the case of TiPtSn, work reported by Kimura et al.[44] determined the alloy to have an n-type behavior. However, our highest value of the PF graph is for a p-type kind of TE. Thus, we include both p and n transport while reporting the data. With change in temperature, the Seebeck coefficient of TiPtSn shows an increasing trend for p-type and a decreasing trend for n-type carrier, irrespective of the carrier concentration, right panel of Figure 5. At ambient conditions and $n_c \sim 1 \times 10^{20}$, S for p and n carriers is computed to be +140 μV/K and −85 μV/K, respectively, values which are significantly different from the one reported by Kimura et al.,[44] who reported an $S = -500$ μV/K at 300 K and presumably at $n_c \sim 1 \times 10^{22}$ cm^{-3}. If we investigate low carrier concentration, $n_c \sim 1 \times 10^{18}$ cm^{-3}, we find a n-type Seebeck value of −460 μV/K. Furthermore,

Table 2. p-Type; Dimensionless TE figure of merit, ZT, Evaluated for TiMSn, (M = Ni , Pd, and Pt) Alloys for Specified Carrier Concentration and Temperature[a]

alloy	n (cm^{-3})	T (K)	PF/τ (W/m K^2 $\times 10^{11}$)	ZT
TiNiSn	1×10^{18}	300	0.40	0.03
		600	0.50	0.05
	1×10^{19}	300	1.4	0.11
		700	2.4	0.28
	1×10^{20}	300	2.2	0.17
		700	6.4	0.75
TiPdSn	1×10^{18}	300	0.34	0.02
		700	0.45	0.05
	1×10^{19}	300	1.38	0.06
		700	2.20	0.20
	1×10^{20}	300	2.00	0.08
		700	5.80	0.34
TiPtSn	2×10^{17}	300	0.11	0.01
		800	0.14	0.02
	1×10^{18}	300	0.34	0.02
		900	0.52	0.07
	1×10^{20}	300	3.00	0.12
		1000	9.10	0.52

[a]The lattice thermal conductivity k_{ph} is 6 W m^{-1} K^{-1} from refs 37 and 44 and ref 42 for the three systems, respectively, while k_{el} is from our computed data. Relaxation time is fixed at $\tau = 1 \times 10^{-14}$ s or 10 fs.

similar to ref 44, we also notice the transition to p-type behavior at 1200 K ($\approx$1100 K for Kimura et al.) for $n_c \sim 2 \times 10^{17}$ cm^{-3}. However, this is quite unrealistic as low concentration corresponds to a chemical potential of 5−6 eV which is far below the Fermi level of this system.

With our calculated power factors, we can estimate the dimensionless figure of merit for these family of alloys. The figure of merit is described as $ZT = S^2\sigma T/k_{total}$, where k_{total} is the total thermal conductivity, sum of the electronic (el) and phononic (ph) contributions and T is temperature in kelvin. Assuming the phononic thermal conductivity from literature data and using our own calculations for k_{el}, we calculate ZT in chosen carrier concentrations, for p and n-type TEs, respectively, Tables 2 and 3.

The total thermal conductivity of TiNiSn is 4−6 W m^{-1} K^{-1} for 300−700 K taken from experimental measurements as in ref 45. At our peak carrier concentration $n \sim 1 \times 10^{20}$ cm^{-3},

Table 3. n-Type; Dimensionless TE Figure of Merit, ZT, Evaluated for TiMSn, (M = Ni, Pd, and Pt) Alloys for Specified Carrier Concentration and Temperature[a]

alloy	n (cm^{-3})	T (K)	PF/τ (W/m K^2 × 10^{11})	ZT
TiNiSn	1×10^{18}	300	0.45	0.03
		600	0.62	0.06
	1×10^{19}	300	1.2	0.09
		700	2.5	0.29
	1×10^{20}	300	1.0	0.08
		700	4.3	0.50
TiPtSn	2×10^{17}	300	0.16	0.01
		800	0.17	0.02
	1×10^{18}	300	0.50	0.02
		700	0.57	0.06
	1×10^{20}	300	1.10	0.04
		900	7.50	0.71

[a]The lattice thermal conductivity k_{ph} is 6 W m^{-1} K^{-1} from refs 37 and 44 and ref 42 for the three systems, respectively, while k_{el} is from our computed data. Relaxation time is fixed at $\tau = 1 \times 10^{-14}$ s or 10 fs.

assuming $k_{\text{total}} = 6$ W m^{-1} K^{-1}, we obtain a ZT of 0.75, which indicates that TiNiSn is likely to be a good p-type TE at 700 K. Assuming an n-type behavior at the same n concentration and T, we arrive at a ZT of 0.50, which is in agreement with most values from literature.[14,46,47]

For TiPdSn, only p-type transport is reported. The highest ZT is 0.34 at $n \sim 1 \times 10^{20}$ cm^{-3} and $T = 700$ K. This value is not in agreement with ref 35 who report the highest ZT value of 0.74 at 500 K, and discrepancies can possibly be ascribed to a difference in the value of computed band gap in addition to the different value of τ, as already mentioned.

For TiPtSn, similar to that reported by Kimura et al.,[44] we have low values of ZT, irrespective of the T, for $n_{\text{c}} < 1 \times 10^{18}$ cm^{-3}, and then, as n_{c} rises up to 1×10^{20} cm^{-3}, ZT reaches a maximum value of 0.71 at 900 K.

Summarizing, our calculations confirm large power factors for all three compounds. It is well known that using techniques such as the phonon glass electron crystal, it is possible to moderate the k_{total} and hence increase their ZT and consequently enhance their TE performance.[48,49]

3.4. Modeling Defects in TiNiSn. In this section, we address the disparity in the experimentally measured and computationally attained band gap for TiNiSn HH alloy. While the experimental band gap is at 0.12 eV,[37] this value was never reproduced in computational studies, irrespective of the computational method or DFT functional used.[13,43]

In our work, we compute a band gap of 0.48 eV with PBE functional that is still four times larger than the experimental one. However, there is the possibility that real materials, which contain defects, may have localized states in the density of states (DOS) that lead to a significant decrease in the band gap. This approach, which may explain the discrepancy

between DFT and experimentally measured energy gap, was proposed and successfully tested by several authors.[13−15,17] In particular, Colinet et al.[13] and Jund and Berche[14] computed a sensitive drop of the band gap when an interstitial Ni was introduced in the pure HH TiNiSn, and in a recent publication, Kirievsky et al.[17] reproduced the same effect modeling, among the others, composition conserving defects.

We adopted an analogous approach by studying two anti-site composition conserving Ni defects in a 2 × 2 × 2 super-cell of the primitive HH cell (24 atoms) at the PBE10/$P.def2$-SVP level. These defects, which preserve the symmetry of the $F\bar{4}3m$ space group, have the lowest formation energy among those calculated,[17] and it can therefore be assumed that they are quite widespread in the experimental samples.

Thus, a single Ni atom is removed from its HH position [−3/8, 1/8, 1/8] and inserted in one of the two vacant Wyckoff positions 8c with fractional coordinates [3/4, 3/4, 3/4] and [1/4, 1/4, 1/4], respectively, obtaining two defect models W8c-333 and W8c-111. Both these sites are occupied in the full-Heusler (FH) TiNi$_2$Sn crystal structure; thus, essentially, we have only displaced a Ni from its original HH site to a FH site, as can be seen in Figure 1 of Supporting Information.

The formation energy of the defects, ΔE_{f}, is evaluated according to equation

$$\Delta E_{\text{f}} = E_{\text{el}}^{\text{defect}} - E_{\text{el}}^{\text{perfect}} \tag{1}$$

where E_{el} is the electronic energy/per atom of the perfect ordered stoichiometric compound and of the W8c-333/W8c-111 systems. If the atoms in the supercell are not relaxed, we obtain ΔE_{f} in the order of 0.6 eV, very close to those computed by other authors for similar defects in HH alloys. In particular, Colinet et al.[13] calculated a formation enthalpy at a PBE level (ignoring the much smaller zero-vibration contribution) of 0.77 eV for an interstitial Ni in a 96 atoms supercell of TiNiSn. However, if all the atoms in the supercell are allowed to relax, the formation energies drop off and the two defective structures, W8c-333 and W8c-111, become only 0.081 V and 0.066 eV less stable than the perfect HH.

Formation enthalpies at 0 K, $\Delta H(0)$, which take into account the zero-point vibrational contribution, and Gibbs free energies of formation at room temperature, $\Delta G(298)$, accounting for the thermal phonon terms, are reported in Table 4. As already stated by others,[13,17] all these contributions do not change significantly the magnitude of the formation energies for these defects that remain very low.

Structure relaxation yields to small but significant differences in the electronic structure and in the atomic coordination patterns.

In agreement with the already mentioned results, we observe a narrowing in the band gaps which decrease to 0.187 eV in W8c-333 and 0.261 eV in W8c-111, see Figure 1 in Supporting

Table 4. PBE10/$P.def2$-SVP Results for Defect Models[a]

alloy	a	gap	$\Delta H(0)$	$\Delta G(298)$	B_0	c_{11}	c_{12}	c_{44}	ν	Y
TiNiSn$_{2\times2\times2}$	8.36	0.69			138.02	235.58	90.19	60.67	0.297	169.15
W8c-333	8.35	0.19	0.078	0.070	133.48	194.63	104.83	44.51	0.351	120.67
W8c-111	8.34	0.26	0.064	0.060	133.84	205.21	99.10	59.45	0.315	149.38

[a]Lattice parameter **a** in Å. Indirect electronic band gap in eV. Δ, evaluated according to eq 1, are in eV per atom. Enthalpy and Gibbs free energy are defined as follows: $H(0) = E_{\text{el}} + \text{ZPE} + PV$; $G(298) = E_{\text{el}} + \text{ZPE} + E(T)_{\text{vib}} + PV - TS_{\text{vib}}$. Frequencies are computed at Γ point only. Bulk modulus, B_0, elastic constants, c_{11}, c_{12}, c_{44}, Young's modulus, Y, in GPa and Poisson ratio, ν.
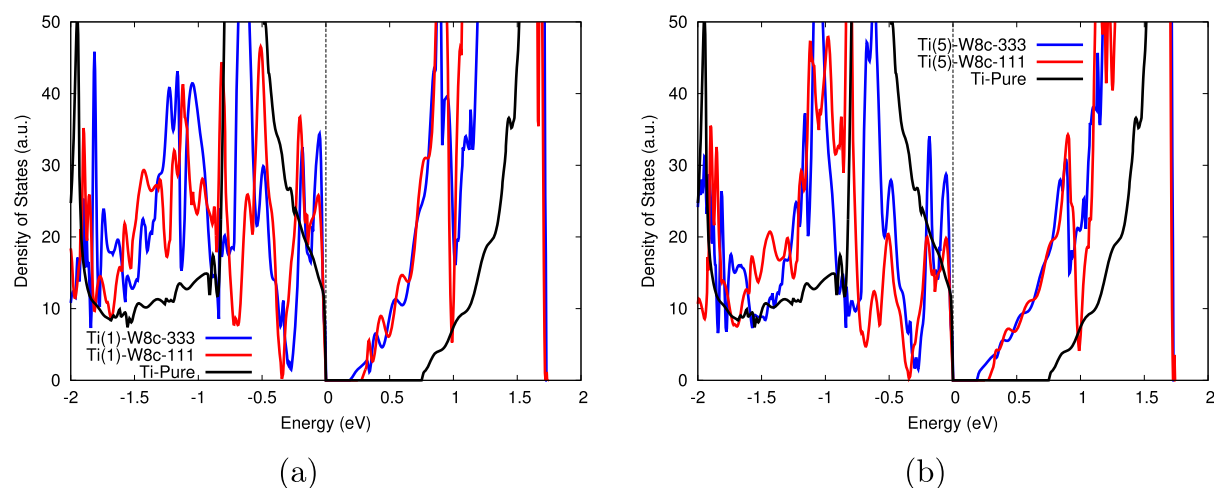
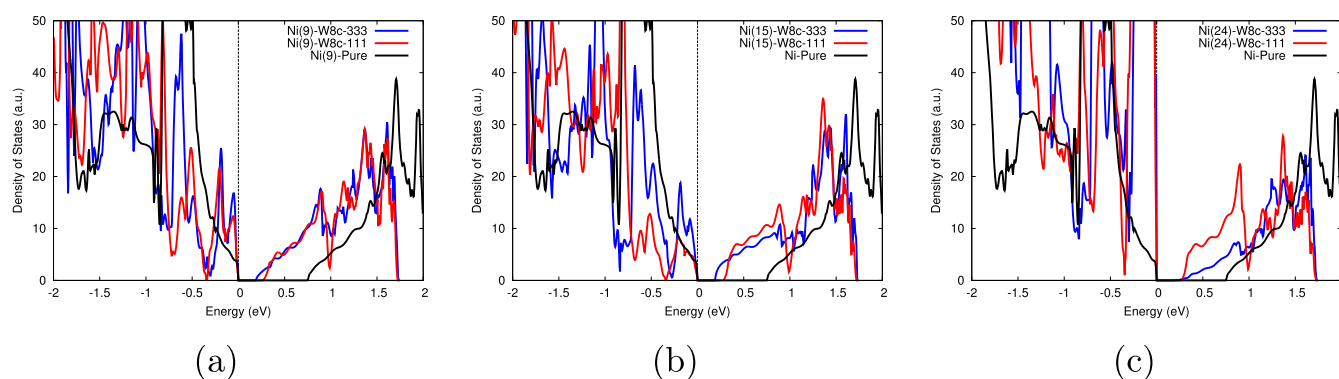**Figure 6.** PDOS on the defect TiNiSn alloys; (a) on Ti(1); (b) on Ti(5).

Figure 7. PDOS on the defect TiNiSn alloys; (a) on Ni(9); (b) on Ni(15); and (c) on Ni(24) the displaced atom.
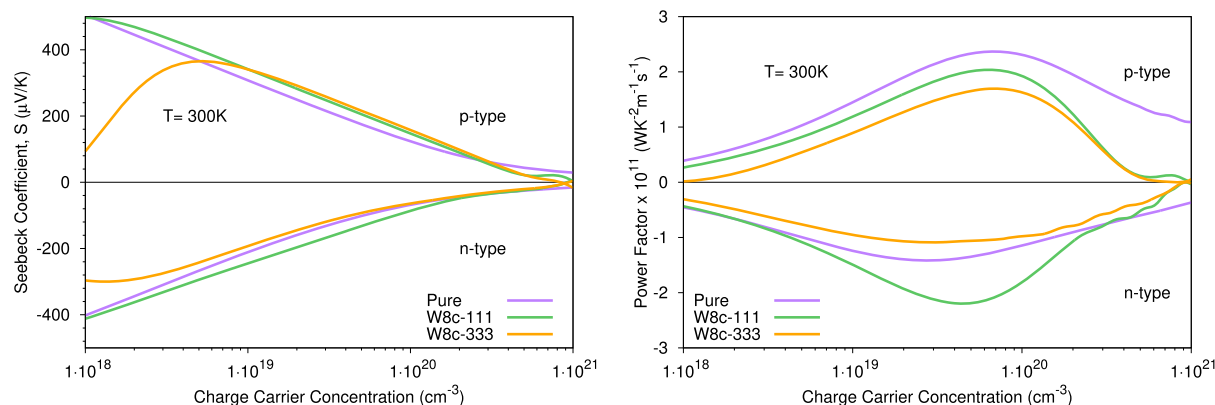

Figure 8. Seebeck coefficient, *S*, and power factor, PF, for perfect TiNiSn, *W8c-333* and *W8c-111* at *T* = 300 K, as a function of the charge carrier concentration, n_c. PF with n-carriers is plotted on the negative axis for clarity.

Information. The antisite Ni atom leads to a localized level in the vicinity of the Fermi level. In particular, the PDOS reveal the presence of Ti−Ni virtual states within the "forbidden region" of the perfect system, see Figures 6 and 7. The projections onto the AOs of Ti(1)/Ti(5) and Ni(9)/Ni(15) present rather similar features in *W8c-111* and *W8c-333* with a net drop of the lowest virtual states with respect to HH TiNiSn. It is worth to mention that the Ni(24) contribution to the lowest unoccupied bands differentiates the two defect systems as it is significantly more pronounced in *W8c-111* than in *W8c-333*, panel (c) of Figure 7. This difference can account

for the different values in some of the TE parameters calculated for the two defect models, as will be shown and discussed in the following.

As the Ni atom is displaced from its HH to a FH position, symmetry related atoms within the 2 × 2 × 2 supercell are no longer equivalent on the basis of different coordination patterns. For example, in *W8c-111*, Ti(1) and Ti(5) have 3 and 5 Ni atoms in the first neighboring shell. while in *W8c-333* Ti(1) and Ti(5), both have four Ni as first neighbors (refer to Tables S1 and S2 of Supporting Information for the adopted notation). Similar behavior is noted for Sn atoms. Interesting

enough, after the geometry optimization, both the defect alloys exhibit Ti(1) with three Ni, at a distance of ≈2.57, and the Ti(5) surrounded by five Ni atoms, including the displaced Ni(24). It seems that atomic rearrangement within the super-cell is driven by the defective Ni which tends to restore its 4-Ti ⊕ 4-Sn octahedral coordination.

Hirshfield charges, collected in Table S2 of Supporting Information, confirm the loss of chemical equivalence among the atoms in the 2 × 2 × 2 defective supercells and sensitive differences among the two models. For *W8c-111*, the increase in Ti(1) atomic charge is particularly evident and is partially compensated by the charge lost by the displaced Ni(24).

Finally, we compare the Seebeck coefficients of the defect models with respect to the pure HH, Figure 8 right panel. At n_c = 1 × 10^{19} cm^{-3}, the absolute value of S for *W8c-333* is considerably lower than the pure HH or *W8c-111*. When considering only p-type carriers, between n_c = 1 × 10^{19} and n_c = 1 × 10^{20} cm^{-3}, the Seebeck coefficient for both defect systems becomes slightly higher than that of the perfect HH. For n-type carriers, *W8c-111* has the highest S in the aforementioned range and converges to the same value as the pure HH only at high n_c values of 1 × 10^{21} cm^{-3}.

In the right panel of Figure 8, we compare the PF of the perfect TiNiSn and the defect systems. *W8c-111* has a power factor almost twice that of the pure system at n_c ∼ 5 × 10^{19} cm^{-3}, for n-type carriers. The electronic contribution to thermal conductivity for this defect system at 300 K is 0.10 W m^{-1} K^{-1}, which is slightly lower than that of the pure TiNiSn (0.15 W m^{-1} K^{-1}). This could explain the enhanced TE properties of *W8c-111* when n-type carriers are considered, and it is consistent with the peculiar antivacant Ni states calculated for this model, see Figure 7.

Hence, by modeling composition conserving Ni defects in TiNiSn, we are able to reproduce rather accurately the expected electronic and TE properties of TiNiSn.

4. CONCLUSIONS

In this work, we used the CRYSTAL code to perform a thorough investigation of the geometry, electronic band structure, and TE properties of three HH alloys: TiNiSn, TiPdSn, and TiPtSn. We described each of these compounds using localized Gaussians and the global hybrid DFT functional PBE10 with 10% HF exchange. Lattice parameters and electronic band structures are correctly reproduced with agreeable band gaps. Next, we computed TE properties—Seebeck coefficient, electrical conductivity, and electronic contribution to the total thermal conductivity within CRYSTAL using a set of basis adapted from the *def2-SVP* and calibrated for periodic calculations.

In TiNiSn, p-type doping shows higher ZT as often noticed in computational studies and in contrast to experimental evidence. Moreover, considering the experimental trend of n-type behavior, we were able to reproduce recognized values of the TE figure of merit. For TiPdSn and TiPtSn, we predicted both alloys to favor p-type transport in their pure single-crystal form and have high room temperature values of power factor at carrier concentrations c_n ∼ 1 × 10^{19} and c_n ∼ 1 × 10^{20} cm^{-3}, respectively. Thus, if the lattice thermal conductivity is carefully controlled, the figure of- merit is expected to be high. Last, we presented two defect TiNiSn models which we believe are a better description of the real material. These defect models feature a Ni atom displaced from its original HH crystallographic site to a vacant FH site. Differences in the

system response to Ni occupying different interstitial sites were found, which were not expected from pure symmetry considerations. Such differences are seen in the band gap, defect formation free energy, and Seebeck coefficients. The power factor of the defect model *W8c-111* prefers n-type carriers and displays almost twice the value for the same without defects. Thus, we were able to systematically reduce the band gap and increase the power-factor for TiNiSn using a more realistic model. The presence of defects is usually not an undesired feature in TEs because it leads to increased phonon scatterings—which in turn lowers the thermal conductivity of the material—thus increasing the ZT value.

■ ASSOCIATED CONTENT

ⓢ Supporting Information

The Supporting Information is available free of charge at https://pubs.acs.org/doi/10.1021/acs.jpcc.0c03243.

Basis set used for the calculations and further details about the defective models (PDF)

■ AUTHOR INFORMATION

Corresponding Authors

Lorenzo Maschio − *Dipartimento di Chimica, Università di Torino, Turin 10125, Italy;* ⓞ orcid.org/0000-0002-4657-9439; Email: lorenzo.maschio@unito.it

Silvia Casassa − *Dipartimento di Chimica, Università di Torino, Turin 10125, Italy;* ⓞ orcid.org/0000-0003-0217-4920; Email: silvia.casassa@unito.it

Authors

Atreyi Dasmahapatra − *Dipartimento di Chimica, Università di Torino, Turin 10125, Italy*

Loredana Edith Daga − *Dipartimento di Chimica, Università di Torino, Turin 10125, Italy*

Antti J. Karttunen − *Department of Chemistry and Materials Science, Aalto University, Espoo 02150, Finland;* ⓞ orcid.org/0000-0003-4187-5447

Complete contact information is available at:
https://pubs.acs.org/10.1021/acs.jpcc.0c03243

Notes

The authors declare no competing financial interest.

■ REFERENCES

(1) *Introduction to Analytical Electron Microscopy*; Hren, J. J. J. D., Goldstein, J. I., Eds.; Springer: Boston (MA), 1979.

(2) Xiao, D.; Yao, Y.; Feng, W.; Wen, J.; Zhu, W.; Chen, X.; Stocks, G.; Zhang, Z. Half-Heusler Compounds as a New Class of Three-Dimensional Topological Insulators. *Phys. Rev. Lett.* **2010**, *105*, 096404.

(3) Lin, H.; Wray, L. A.; Xia, Y.; Xu, S.; Jia, S.; Cava, R. J.; Bansil, A.; Hasan, M. Z. Half-Heusler ternary compounds as new multifunctional

experimental platforms for topological quantum phenomena. *Nat. Mater.* **2010**, *9*, 546.

(4) Shi, X.; Chen, L.; Uher, C. Recent advances in high-performance bulk thermoelectric materials. *Int. Mater. Rev.* **2016**, *61*, 379−415.

(5) Birkel, C. S.; Zeier, W. G.; Douglas, J. E.; Lettiere, B. R.; Mills, C. E.; Seward, G.; Birkel, A.; Snedaker, M. L.; Zhang, Y.; Snyder, G. J.; Pollock, T. M.; Seshadri, R.; Stucky, G. D. Rapid Microwave Preparation of Thermoelectric TiNiSn and TiCoSb Half-Heusler Compounds. *Chem. Mater.* **2012**, *24*, 2558−2565.

(6) Jung, D.-y.; Kurosaki, K.; Kim, C.-e.; Muta, H.; Yamanaka, S. Thermal expansion and melting temperature of the half-Heusler compounds: MNiSn (M = Ti, Zr, Hf). *J. Alloys Compd.* **2010**, *489*, 328−331.

(7) Gelbstein, Y.; Tal, N.; Yarmek, A.; Rosenberg, Y.; Dariel, M. P.; Ouardi, S.; Balke, B.; Felser, C.; Köhne, M. Thermoelectric properties of spark plasma sintered composites based on TiNiSn half-Heusler alloys. *J. Mater. Res.* **2011**, *26*, 1919−1924.

(8) Zou, M.; Li, J.-F.; Du, B.; Liu, D.; Kita, T. Fabrication and thermoelectric properties of fine-grained TiNiSn compounds. *J. Solid State Chem.* **2009**, *182*, 3138−3142.

(9) Gautier, R.; Zhang, X.; Hu, L.; Yu, L.; Lin, Y.; Sunde, T. O. L.; Chon, D.; Poeppelmeier, K. R.; Zunger, A. Prediction and accelerated laboratory discovery of previously unknown 18-electron ABX compounds. *Nat. Chem.* **2015**, *7*, 308.

(10) Legrain, F.; Carrete, J.; van Roekeghem, A.; Madsen, G. K. H.; Mingo, N. Materials Screening for the Discovery of New Half-Heuslers: Machine Learning versus ab Initio Methods. *J. Phys. Chem. B* **2018**, *122*, 625−632.

(11) Carrete, J.; Li, W.; Mingo, N.; Wang, S.; Curtarolo, S. Finding Unprecedentedly Low-Thermal-Conductivity Half-Heusler Semiconductors via High-Throughput Materials Modeling. *Phys. Rev. X* **2014**, *4*, 011019.

(12) Hazama, H.; Matsubara, M.; Asahi, R.; Takeuchi, T. Improvement of thermoelectric properties for half-Heusler TiNiSn by interstitial Ni defects. *J. Appl. Phys.* **2011**, *110*, 063710.

(13) Colinet, C.; Jund, P.; Tédenac, J.-C. NiTiSn a Material of Technological Interest: Ab Initio Calculations of Phase Stability and Defects. *Intermetallics* **2014**, *46*, 103−110.

(14) Berche, A.; Jund, P. Fully Ab initio determination of the Thermoelectric properties of Half-Heusler NiTiSn: Crucial role of interstitial Ni Defects. *Materials* **2018**, *11*, 868.

(15) Rittiruam, M.; Yangthaisong, A.; Seetawan, T. Enhancing the Thermoelectric Performance of Self-Defect TiNiSn: A First-Principles Calculation. *J. Electron. Mater.* **2018**, *47*, 7456−7462.

(16) Ren, W.; Zhu, H.; Mao, J.; You, L.; Song, S.; Tong, T.; Bao, J.; Luo, J.; Wang, Z.; Ren, Z. Manipulation of Ni Interstitials for Realizing Large Power Factor in TiNiSn-Based Materials. *Adv. Electron. Mater.* **2019**, *5*, 1900166.

(17) Kirievsky, K.; Fuks, D.; Gelbstein, Y. Composition conserving defects and their influence on the electronic properties of thermoelectric TiNiSn. *Phys. Chem. Chem. Phys.* **2020**, *22*, 8035.

(18) Kirievsky, K.; Shlimovich, M.; Fuks, D.; Gelbstein, Y. An ab initio study of the thermoelectric enhancement potential in nano-grained TiNiSn. *Phys. Chem. Chem. Phys.* **2014**, *16*, 20023−20029.

(19) Dovesi, R.; Erba, A.; Orlando, R.; Zicovich-Wilson, C. M.; Civalleri, B.; Maschio, L.; Rérat, M.; Casassa, S.; Baima, J.; et al. Quantum-mechanical condensed matter simulations with CRYSTAL. *Wiley Interdiscip. Rev.: Comput. Mol. Sci.* **2018**, *8*, No. e1360.

(20) Guss, P.; Foster, M. E.; Wong, B. M.; Patrick Doty, F.; Shah, K.; Squillante, M. R.; Shirwadkar, U.; Hawrami, R.; Tower, J.; Yuan, D. Results for aliovalent doping of CeBr3 with Ca2+. *J. Appl. Phys.* **2014**, *115*, 034908.

(21) Mikaeilzadeh, L.; Tavana, A.; Khoeini, F. Electronic structure of the PrNiBi half-Heusler system based on the σ GGA+ U method. *Sci. Rep.* **2019**, *9*, 20075.

(22) Sansone, G.; Ferretti, A.; Maschio, L. Ab initio electronic transport and thermoelectric properties of solids from full and range-separated hybrid functionals. *J. Chem. Phys.* **2017**, *147*, 114101.

(23) Perdew, J. P.; Burke, K.; Ernzerhof, M. Generalized gradient approximation made simple. *Phys. Rev. Lett.* **1996**, *77*, 3865.

(24) Corà, F.; Alfredsson, M.; Mallia, G.; Middlemiss, D.; Mackrodt, W.; Dovesi, R.; Orlando, R. *Principles and Applications of Density Functional Theory in Inorganic Chemistry II*; Springer: Heidelberg, pp 171−232.

(25) Weigend, F.; Ahlrichs, R. Balanced basis sets of split valence, triple zeta valence and quadruple zeta valence quality for H to Rn: Design and assessment of accuracy. *Phys. Chem. Chem. Phys.* **2005**, *7*, 3297−3305.

(26) Daga, L. E.; Civalleri, B.; Maschio, L. Gaussian Basis Sets for Crystalline Solids: All-Purpose Basis Set Libraries vs System-Specific Optimizations. *J. Chem. Theory Comput.* **2020**, *16*, 2192−2201.

(27) Perdew, J. P.; Ernzerhof, M.; Burke, K. Rationale for mixing exact exchange with density functional approximations. *J. Chem. Phys.* **1996**, *105*, 9982−9985.

(28) Adamo, C.; Barone, V. Toward reliable density functional methods without adjustable parameters: The PBE0 model. *J. Chem. Phys.* **1999**, *110*, 6158−6170.

(29) Dovesi, R.; et al. *CRYSTAL17 User's Manual*, 2017.

(30) Shanno, D. F. Conditioning of quasi-Newton methods for function minimization. *Math. Comput.* **1970**, *24*, 647.

(31) Zicovich-Wilson, C. M.; Dovesi, R. On the use of symmetry adapted crystalline orbitals in SCF-LCAO periodic calculations. I. The construction of the symmetrized orbitals. *Int. J. Quantum Chem.* **1998**, *67*, 299.

(32) Erba, A.; Mahmoud, A.; Belmonte, D.; Dovesi, R. High pressure elastic properties of minerals from ab initio simulations: The case of pyrope, grossular and andradite silicate garnets. *J. Chem. Phys.* **2014**, *140*, 124703.

(33) Öğüt, S.; Rabe, K. M. Band gap and stability in the ternary intermetallic compounds NiSnM (M= Ti, Zr, Hf): A first-principles study. *Phys. Rev. B* **1995**, *51*, 10443.

(34) Klimm, D.; Paufler, P. Point defects in GaP single crystals investigated by mechanical damping. *Cryst. Res. Technol.* **1987**, *22*, 1023−1030.

(35) Kaur, K. TiPdSn: A half Heusler compound with high thermoelectric performance. *Europhys. Lett.* **2017**, *117*, 47002.

(36) Roy, A.; Bennett, J. W.; Rabe, K. M.; Vanderbilt, D. Half-Heusler semiconductors as piezoelectrics. *Phys. Rev. Lett.* **2012**, *109*, 037602.

(37) Aliev, F. G.; Kozyrkov, V. V.; Moshchalkov, V. V.; Scolozdra, R. V.; Durczewski, K. Narrow band in the intermetallic compounds MNiSn (M=Ti, Zr, Hf). *Z. Phys. B: Condens. Matter* **1990**, *80*, 353−357.

(38) Rogl, G.; Grytsiv, A.; Gürth, M.; Tavassoli, A.; Ebner, C.; Wünschek, A.; Puchegger, S.; Soprunyuk, V.; Schranz, W.; Bauer, E.; Müller, H.; Zehetbauer, M.; Rogl, P. Mechanical properties of half-Heusler alloys. *Acta Mater.* **2016**, *107*, 178−195.

(39) Bhattacharya, S.; Pope, A. L.; Littleton, R. T.; Tritt, T. M.; Ponnambalam, V.; Xia, Y.; Poon, S. J. Effect of Sb doping on the thermoelectric properties of Ti-based half-Heusler compounds, TiNiSn$_{1−x}$Sb$_x$. *Appl. Phys. Lett.* **2000**, *77*, 2476−2478.

(40) Kim, K. S.; Kim, Y.-M.; Mun, H.; Kim, J.; Park, J.; Borisevich, A. Y.; Lee, K. H.; Kim, S. W. Direct Observation of Inherent Atomic-Scale Defect Disorders responsible for High-performances Ti$_{1−x}$Hf$_x$NiSn$_{1−y}$Sb$_y$ Half-Heusler Thermoelectric Alloys. *Adv. Mater.* **2017**, *29*, 1702091.

(41) Kimura, Y.; Asami, C.; Chai, Y. W.; Mishima, Y. Thermoelectric Performance of Half-Heusler TiNiSn Alloys Fabricated by Solid-Liquid Reaction Sintering. *Mater. Sci. Forum* **2010**, *654−656*, 2795−2798.

(42) Zilber, T.; Cohen, S.; Fuks, D.; Gelbstein, Y. TiNiSn half-Heusler crystals grown from metallic flux for thermoelectric applications. *J. Alloys Compd.* **2019**, *781*, 1132−1138.

(43) Wang, L. L.; Miao, L.; Wang, Z. Y.; Wei, W.; Xiong, R.; Liu, H. J.; Shi, J.; Tang, X. F. Thermoelectric performance of half-Heusler compounds TiNiSn and TiCoSb. *J. Appl. Phys.* **2009**, *105*, 013709.

(44) Kimura, Y.; Zama, A.; Mishima, Y. Thermoelectric Properties of P-type Half-Heusler Compounds HfPtSn and ZrPtSn. *25th International Conference on Thermoelectrics*, 2006; pp 115−119.

(45) Aversano, F.; Ferrario, A.; Boldrini, S.; Fanciulli, C.; Baricco, M.; Castellero, A. Thermoelectric Properties of TiNiSn Half Heusler Alloy Obtained by Rapid Solidification and Sintering. *J. Mater. Eng. Perform.* **2018**, *27*, 6306−6313.

(46) Downie, R. A.; Maclaren, D. A.; Bos, J.-W. G. Thermoelectric performance of multiphase XNiSn (X = Ti, Zr, Hf) half-Heusler alloys. *J. Mater. Chem. A* **2014**, *2*, 6107−6114.

(47) Muta, H.; Kanemitsu, T.; Kurosaki, K.; Yamanaka, S. High-temperature thermoelectric properties of Nb-doped MNiSn (M = Ti, Zr) half-Heusler compound. *J. Alloys Compd.* **2009**, *469*, 50−55.

(48) Rowe, D. M. *CRC Handbook of Thermoelectrics*; CRC press, 2010.

(49) Sales, B. C. Electron Crystals and Phonon Glasses: A New Path to Improved Thermoelectric Materials. *MRS Bull.* **1998**, *23*, 15−21.